A Numerical Comparison of Precipitating Turbulent Flows Between Large-Eddy Simulation and One-Dimensional Turbulence

Alex W. Abboud, Ben B. Schroeder, Tony Saad, and Sean T. Smith
Dept. of Chemical Engineering, Institute for Clean and Secure Energy, University of Utah, Salt Lake City, UT 84112

Derek D. Harris and David O. Lignell
Dept. of Chemical Engineering, Brigham Young University, Provo, UT 84602

DOI 10.1002/aic.14870
Published online May 19, 2015 in Wiley Online Library (wileyonlinelibrary.com)

This study presents the results of computational fluid dynamics simulations of a multiphase, reacting, turbulent mixing layer in an idealized geometry. The purpose is to compare large-eddy simulation (LES) to one-dimensional turbulence (ODT) and examine the trends of the flow under differing mixing conditions. Aqueous streams are mixed together to precipitate polymorphs of calcium carbonate. The polymorphs of calcium carbonate are tracked numerically using population balance equations (PBE). Each PBE contains all of the relevant physical models to track the particle evolution including nucleation, growth, and aggregation. A simple subgrid mixing model that is convenient for use with PBEs was implemented in the LES code. The higher spatial resolution achievable with ODT allowed an investigation on the effect of resolution on the mixing-model error. The Reynolds number of the flow is varied and is shown to cause a decrease in average particle sizes with higher mixing rates. © 2015 American Institute of Chemical Engineers *AIChE J*, 61: 3185–3197, 2015

Keywords: LES, QMOM, ODT, DQMOM, precipitation modeling

Introduction

There are many computational fluid dynamics (CFD) methods in the literature. Direct numerical simulation (DNS) is widely regarded as the most accurate method, but it quickly runs into limitations of computational time and domain size. Reynolds-Averaged Navier-Stokes (RANS) lies at the other end of the computational cost. Although it may be computationally inexpensive to run simulations with RANS, many types of flows can exhibit low accuracy. There are several methods in the intermediate range which attempt to balance accuracy with computational cost for specific flows. Two of these intermediate methods will be studied here: large-eddy simulation (LES) and one-dimensional turbulence (ODT). LES maintains a detailed description of three-dimensional flow domains by resolving only the largest eddies in the system while modeling the subgrid scales.[1] ODT maintains a full spatial resolution of the flow in one spatial dimension and models, with stochastic methods, the effects of turbulent advection.[2] As ODT resolves only one dimension spatially, it can be less computationally costly than LES when using the same resolution. Due to this, the ODT simulations in this study are run at a higher spatial resolution than that of the LES ones. The downside here is that the ODT formulation requires the use of a simple geometric configurations

A temporal jet flow is used to examine the influence of the Reynolds number and mixing on reactions in the shear layers between the two streams. This simple flow setup allows for good results from the ODT code. The use of an idealized mixing layer to examine reactions in CFD has been studied in DNS by Riley et al.[3,4] and more recently by Pantano et al.[5] A similar study using LES examined the use of different subgrid models in a turbulent mixing layer from an idealized temporal jet.[6] The use of a temporal jet to study an elementary reaction in a LES mixing layer was reported by Colucci et al.[7] A turbulent mixing layer has also been used in more recent simulations for DNS simulations of soot formation[8] and flame extinction.[9] In addition, studies have been conducted with this geometry to compare ODT results to DNS results for extinction[10] and for soot formation.[11]

Sodium-carbonate and calcium-chloride salts are both soluble in water, and when mixed together, make a supersaturated solution for the precipitation of calcium carbonate. For the conditions used in this study, calcium carbonate precipitates as one (or more) of four distinct solid phases. These solid phases are loosely referred to as polymorphs, the polymorphs are amorphous calcium carbonate (ACC), vaterite, aragonite, and calcite. ACC is the most unstable phase and has a solubility orders of magnitude lower than the other forms. It is theorized that this phase rapidly precipitates and redissolves back into solution once its supersaturation ratio drops.[12] Of the three

Correspondence concerning this article should be addressed to A. W. Abboud at awabboud@yahoo.com or S. T. Smith at sean.t.smith@utah.edu.

© 2015 American Institute of Chemical Engineers

remaining polymorphs, vaterite and aragonite are metastable, while calcite is the most stable form. The temperature of the system affects the solubilities of all four polymorphs, and it provides the strongest effect on the long time preference in the competition between the metastable phases of vaterite and aragonite or the stable phase of calcite.[13] The simulations in this study are run at room temperature; at this condition ACC and calcite should be the most abundant phases.

In order to track the properties of the precipitating solid phases, a population balance approach is utilized. This approach consists of tracking the distribution of solid particles via a population balance equation (PBE). The PBE formalism allows one to accurately account for the various solid phase interactions with appropriate physical models. One PBE is used for each of the four polymorphs of calcium carbonate. A moment method is used to circumvent the many challenges associated with the direct solution of PBEs. The moment method provides a suitable way to track the statistics of the PBE, but requires some closure for the source terms.[14,15] Using a PBE approach, Schroeder et al.[16] have shown that the physical models can reproduce experimental results by Ogino et al.[12] for a simple spatially homogeneous problem of calcium carbonate precipitation.

The idealized flow regime with a mixing layer allows for the comparison between LES and ODT simulations. The ODT was run at a much higher resolution, and will be used as a baseline for the comparison. As the temporal jet used here is a simple geometry, the ODT should be able to give good flow results at a high resolution. The article is organized as follows, first, the theory used for the population balances and the associated particle source terms will be discussed. Then the setup for both of the numerical sets of simulations for LES and ODT will be outlined. This is followed by a detailed comparison of the the LES and ODT results. Finally, due to the high resolution of the ODT simulations it will be used to perform an analysis of the subgrid mixing model than is used in the LES code.

Theory and Setup

The flow setup used in this study is a turbulent mixing layer with periodic boundary conditions in all directions. The physical domain size is 0.04 m by 0.02 m by 0.02 m with a central jet width of 0.01 m. This central jet is initialized to a mixture fraction of 1, with a velocity of U_0, with the rest of the domain initialized to a mixture fraction of 0, with a velocity of $-U_0$. The initial case is run with $U_0 = 0.75$ m/s and $T = 25°C$, with a Reynolds number of 16,000. The Reynolds number is increased in the additional simulations to 64,000 and 128,000, corresponding to $U_0 = 3.0$ m/s and $U_0 = 6.0$ m/s, respectively. This simple geometry is used, as the ODT code has difficulty in simulating flows which are not canonical. This geometry would be representative of the early mixing regions of a full scale reactor.

In this system an initial concentration of 0.03 M in each of the pure streams of the jets is used, these streams are aqueous sodium carbonate and calcium chloride. At this low concentration, using Davies' correlations for activity coefficients has been shown to perform well.[17] Aqueous phase equilibrium equations are solved for 10 of the major species in solution. The supersaturation ratio for each polymorph is calculated based on the aqueous chemical activities and known solubilities for each polymorph, α, as $S_\alpha = [CaCO_3]/[CaCO_3]_{eq,\alpha}$.[13] The simulation time steps are much higher than the aqueous reaction speed, so utilizing an equilibrium approach should be a good assumption. In the LES code, the aqueous chemistry is tabulated over mixture fraction and extent of reaction prior to running the CFD simulations to avoid the computational cost of solving the nonlinear system of equations. The supersaturation data are well behaved, and 21 discrete points are tabulated for mixture fraction space, and 15 discrete points tabulated for extent of reaction space. The ODT is less computationally expensive and does not use a tabular approach, instead the ODT code calculates the equilibrium concentrations at each point in the domain as the simulation progresses.

Precipitation model

The numerical model for the particles consists of transporting the particle size distribution (PSD), as demonstrated by Randolph.[18] The PSD is adapted here to contain all of the complex source terms

$$\frac{D\eta(r)}{Dt} + \frac{\partial G(r)\eta(r)}{\partial r} = B(r) + A(r) + \xi_{mix} + D(r) \tag{1}$$

PSDs are commonly used in the crystallization community and have been shown to accurately represent populations of particles.[19–21] The model used in this study consists of a full development of physical terms for the birth (B), death (D), growth (G), and aggregation (A) kernels, along with a term for subgrid mixing in the LES (ξ_{mix}) . Equation 1 is transformed into an equation for the moments of the distribution by multiplying by r^k, where k is the order of the moment, and integrating. The kth moment is defined by $m_k = \int_0^\infty r^k \eta(r) dr$. The moment transport equation can then be expressed as

$$\frac{Dm_k}{Dt} + k\int_0^\infty r^{k-1} G(r)\eta(r) dr = \int_0^\infty r^k (B(r) + A(r) + \xi_{mix} + D(r)) dr \tag{2}$$

Using a moment method requires closure of integral terms. In the LES code QMOM is used.[14] The closure model defines weights and abscissas such that

$$m_k = \sum_{i=1}^{N} w_i R_i^k \tag{3}$$

The weights, w_i, and abscissas, R_i, are solved using the product-difference algorithm.[22] For each of the polymorphs, six moments are transported which results in three abscissas and weights. In order to help maintain numerical stability, the domain is initialized with a small uniform distribution of 1 billion particles per cubic meter with an average size of 500 nm.

In Schroeder et al.,[16] a comprehensive modeling scheme for this precipitate system was developed. It was shown that this scheme could describe the experimental results from Ogino et al.[12] A brief summary of the models used in the simulations is listed, but for a more in depth guide refer to Schroeder et al.[16]

The PBE uses a corrected homogeneous birth model[23–25] to nucleate particles at a given critical radius.[26] The growth term used is a simple bulk diffusion growth at high supersaturation,[26–28] and kinetically limited growth at low supersaturation[29–31] with a correction for Ostwald ripening included in both terms.[26,32] A term for the aggregation of the particles is also included,[33] with a correction for collision efficiency.[34] Lastly, an internally developed empirical model for death of small particles is included.[16] Table 1 shows a list of the actual formulas used for this set of precipitation models.

For the birth rate, z is the Zeldovich factor, k_f is the the reaction rate coefficient, N_1 is the molecules in solution, ΔG is the

Table 1. Models Used in the PBE

Type	Formula	
Birth	$J = zk_f N_1^2 \exp(\Delta G/K_b T)$	(4)
Critical radius	$r_c = \frac{2\sigma_T v}{RT\ln(S)}$	(5)
Growth	$G(r) = vDC_{\mathrm{eq}}(S-\bar{S})/r$	(6)
Growth at low S	$G(r) = -k_s(S-\bar{S})^2$	(7)
Ostwald ripening	$\bar{S} = \exp(2\sigma_T v/RTr)$	(8)
Aggregation	$A_i = 1/2\sum_i w_i \sum_j w_j (r_i^3+r_j^3)^{\alpha/3}\beta_{ij}\psi_{ij} - \sum_i r_i^{\alpha} w_i \sum_j \beta_{ij}\psi_{ij} w_j$	(9)
Aggregation frequency	$\beta_{ij} = \frac{2K_b T}{3\rho}\frac{(r_i+r_j)^2}{r_i r_j} + \frac{4}{3}\left(\frac{3\pi\epsilon}{10v_{\mathrm{fluid}}}\right)^{1/2}(r_i+r_j)^3$	(10)
Aggregation efficiency	$\psi_{ij} = \frac{m_1}{1+m_1},\ m_1 = \begin{cases} G(r_i) \geq G(r_j) & \frac{LG(r_i)}{\rho\epsilon d^2} \\ \text{else} & \frac{LG(r_j)}{\rho\epsilon d^2} \end{cases}$	(11)
Death	$D_i = -30k_D w_i/\Delta t$	(12)

Gibbs free energy, K_b is the Boltzmann constant and T is the temperature. For critical radius, σ_T is the Tolman surface energy, v is the molecular volume, R is the gas constant, and S is the supersaturation ratio. For the growth rates, D is the diffusion coefficient, C_{eq} is the equilibrium concentration, and k_s is an empirical rate constant. The aggregation frequency is a combination of turbulent aggregation and Brownian kernels, with v as the fluid viscosity and ϵ as the dissipation. For the aggregation efficiency kernel, L is a empirical length parameter and d is the average particle diameter of the colliding particles. For the death rate, k_D is a correlated rate coefficient.

It should be noted that the model used here makes a few simplifications to avoid the effects of ion ratio,[35–38] pH levels,[39,40] the direct transformation of polymorphs,[41,42] and non-classical nucleation.[43,44] As the particle volume fraction values are estimated to be low, viscosity effects of the particle-laden solution were neglected.[45,46] Due to the modularity of the model described here, more advanced physics can be substituted if desired.

Numerical simulation—LES

The LES simulations were run using a C++ computational framework called Uintah, which was developed for large-scale parallelization of physics components.[47–49] The Uintah code is maintained in a repository which allows for free distribution.[50] There are multiple components to the Uintah framework, two of which are utilized here. The Uintah framework handles the parallelization of the code, while the components deal with the solution to the velocity and scalar fields. For these simulations, the ARCHES component of the framework solves the conservative, finite-volume, low-Mach formulation of the Navier-Stokes equations with a pressure projection that includes the effects of variable density, reaction, and heat transfer models in the gas phase.[51,52] Here, ARCHES is applied to the LES of liquid mixing and transport. The Wasatch component of the Uintah framework was utilized in a hybrid code-base for the PBEs of the simulation.[53] For the spatial filtering in LES, a simple box filter is used.

The LES simulations contain 8.2 million cells as 320 × 160 × 160 equally spaced grid points and are run in parallel on 1024 processors. The domain is periodic in all three dimensions. Spatial discretization is carried out using a second-order scheme while temporal discretization uses a second-order, strong stability preserving time integrator. The initial condition for LES is shown in Figure 1, along with the mixture fraction profile at different snapshots in time. The central jet is set at a velocity of U_0 with a mixture fraction of 1.0—pure aqueous calcium chloride, the outer jet is set at a velocity of $-U_0$ and a mixture fraction of 0.0—pure aqueous sodium carbonate. For subgrid modeling of the stresses, the dynamic Smagorinsky model was used.[54] Each case was run for 48 h of computational time to ensure a well-mixed state was reached. This resulted in a simulation time of just over 0.4 s. With the jet time scale defined as $\tau_j = H_0/\Delta U$, the number of jet times is equivalent to 60 for the lowest Reynolds number and increases to 240 and 480 for the other two cases.

Subgrid Mixing Model. On the subgrid scale, the mixing is represented by three distinct environments: pure stream 1 of aqueous calcium chloride, pure stream 2 of aqueous sodium carbonate, and a mixed portion where the precipitation of calcium carbonate occurs. No reactions or precipitation occur in the pure stream environments. This approach is used over a direct quadrature method of moments using interaction by exchange with the mean (DQMOM)-IEM approach[55] due to the inexpensive computational cost. The mixture fraction and the scalar variance are calculated at each grid point. Using the constraint of 3 delta functions, analytical solutions are found for the weights of each of the three environments in the subgrid scale as

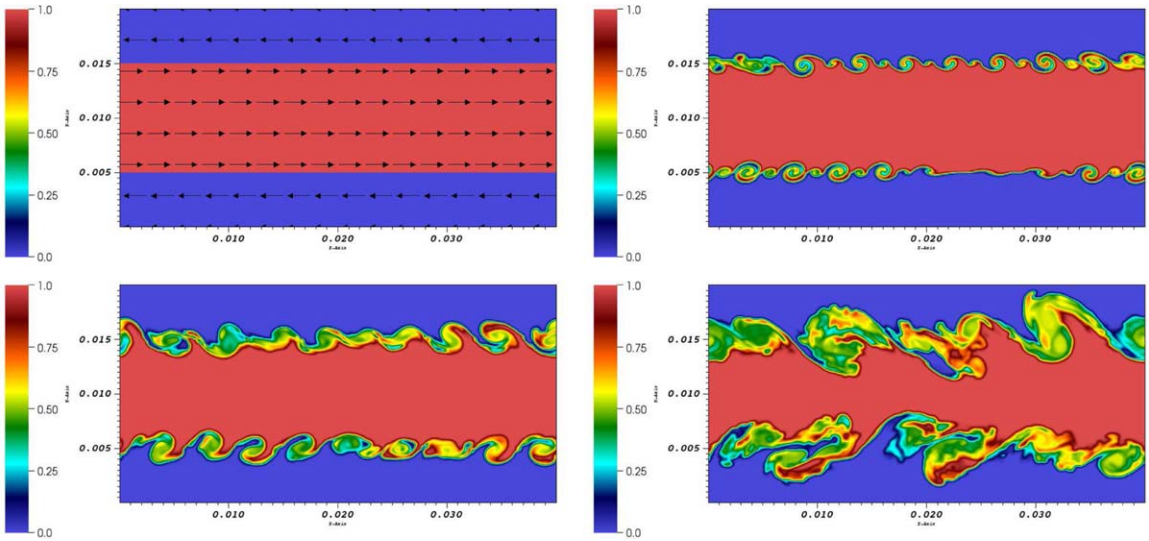

Figure 1. Domain initialization and progression while mixing in the LES.

The colorbar corresponds to mixture-fraction values. In the center jet, mixture fraction is initialized to 1.0 and velocity to U_0; in the outer jet, mixture fraction is initialized to 0.0 and velocity to $-U_0$. [Color figure can be viewed in the online issue, which is available at wileyonlinelibrary.com.]

$$\omega_1 = \frac{\tilde{Z''^2}}{\tilde{Z}} \tag{13}$$

$$\omega_2 = \frac{\tilde{Z''^2} - \tilde{Z} + \tilde{Z}^2}{\tilde{Z}^2 - \tilde{Z}} \tag{14}$$

$$\omega_3 = \frac{-\tilde{Z''^2}}{\tilde{Z} - 1} \tag{15}$$

Here ω_i is the weight of each environment, $\tilde{Z}$ is the average mixture fraction, and $\tilde{Z''^2}$ is the average mixture fraction variance in the cell. The PBE is only solved in the middle environment, ω_2. The moments in environments 1 and 3 are initialized to the same non-zero value as the rest of the domain and are held constant throughout the simulation. The source term that appears in the PBE due to mixing environments 1 and 3 into the center is

$$\Xi_{\text{mix}} \equiv \int_0^\infty \xi_{\text{mix}} r^k \mathrm{d}r \tag{16}$$

$$\Xi_{\phi_{k,2},mix} = -\frac{\mathrm{d}\omega_1/\mathrm{d}t}{\omega_2}(\phi_{k,1} - \phi_{k,2}) - \frac{\mathrm{d}\omega_3/\mathrm{d}t}{\omega_2}(\phi_{k,3} - \phi_{k,2}) \tag{17}$$

Here $\phi_{k,i}$ represents the kth moment for the ith environment, so $\phi_{k,2}$ is the main solution variable, while $\phi_{k,1}$ and $\phi_{k,3}$ are constant at the initialized value. The time derivative terms in Eq. 17 are given by

$$\frac{\mathrm{d}\omega_1}{\mathrm{d}t} = \frac{-\chi_Z}{\tilde{Z}} \tag{18}$$

$$\frac{\mathrm{d}\omega_3}{\mathrm{d}t} = \frac{-\chi_Z}{1 - \tilde{Z}} \tag{19}$$

Here χ_Z is the scalar dissipation rate. Figure 2 shows the graphical subgrid illustration and the corresponding probability density functions as discrete delta functions for an average mixture fraction of 0.5 with the scalar variance normalized by the maximum.

The derivative terms calculated in Eqs. 18 and 19 both require calculation of the scalar variance. This value is not transported on the grid directly, but calculated based on the transport of the mixture fraction and the second moment of the mixture fraction

$$\tilde{Z''^2} = \tilde{Z^2} - \tilde{Z}^2 \tag{20}$$

The second moment of the mixture fraction then requires a transport equation

$$\frac{\mathrm{D}}{\mathrm{D}t}\left(\bar{\rho}\tilde{Z^2}\right) = \frac{\partial}{\partial x_j}\left(\bar{\rho}(D_Z + D_t)\frac{\partial \tilde{Z^2}}{\partial x_j}\right) - \bar{\rho}\chi_Z \tag{21}$$

Here D_Z and D_t are the molecular and turbulent diffusion coefficients, respectively. This equation requires the closure of the scalar dissipation rate χ_Z for the source term. This is implemented as an approximation based on the mixture fraction gradient[56]

$$\chi_Z \approx 2(D_Z + D_t)\frac{\partial \tilde{Z}}{\partial x_i}\frac{\partial \tilde{Z}}{\partial x_i} \tag{22}$$

Numerical simulation—ODT

The ODT model used in this study has been described in detail by Lignell et al.[57] In this section, a summary of the model formulation is given. ODT solves unsteady equations for mass, momentum, and other scalars in a single spatial dimension. Because turbulence cannot naturally evolve in one-dimension, turbulent advection is modeled stochastically. There are two concurrent processes in ODT: (1) evolution of the unsteady, one-dimensional transport equations (termed the diffusion process), and (2) the modeled advection processes. Turbulent advection is modeled by so-called eddy events in which portions of the domain are remapped using triplet maps.[58] A single eddy is parameterized by a size l, a position y_0, and a timescale τ_e. A triplet map associated with an eddy event consists of taking each scalar profile in the map region $y_0 \le y \le y_0 + l$ and replacing it with three copies of the profile, each spatially compressed by a factor of three, with the center copy spatially inverted. In this process, all scalar quantities are conserved and remain continuous. An eddy event is also consistent with turbulent motions in that it increases scalar gradients and decreases local length scales.

In the vector formulation of ODT[59] used here, kernel operations (in addition to triplet maps) are applied to velocity components to model return-to-isotropy effects.[57,60]

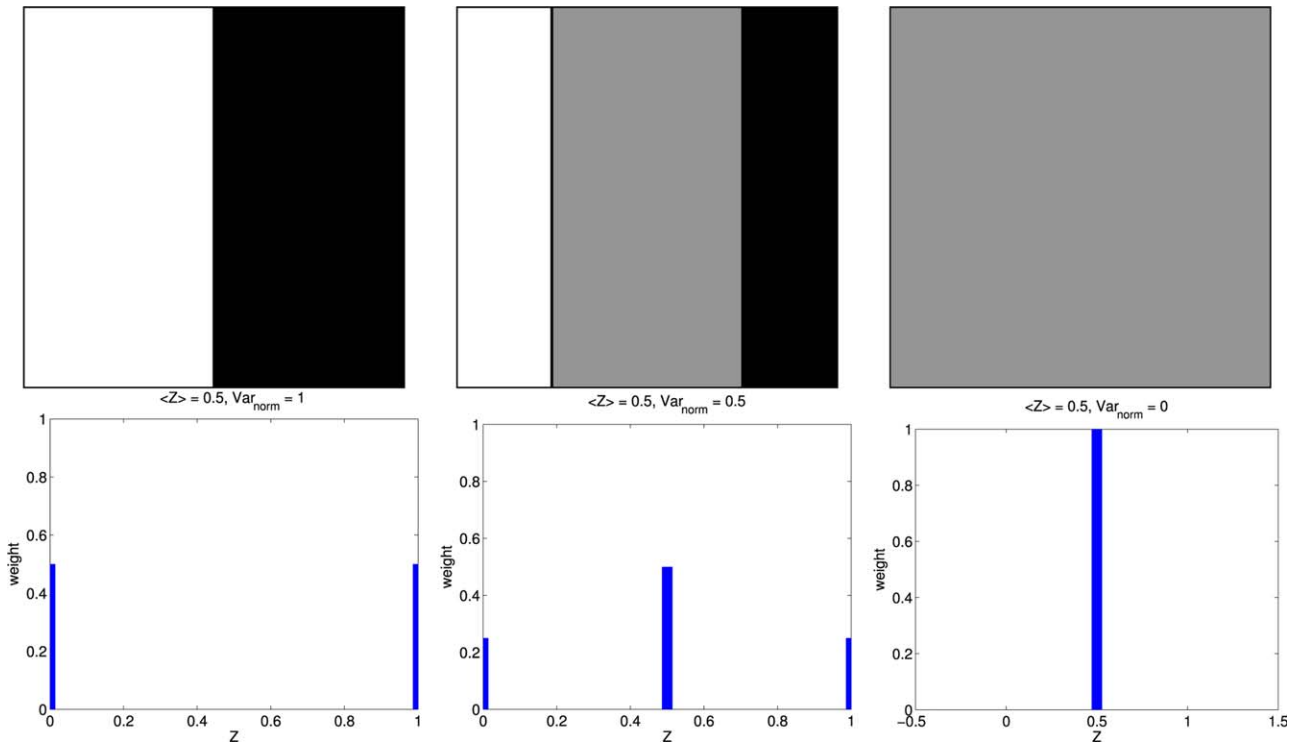

Figure 2. Graphical representations and PDFs of subgrid environment.

The top plots are representative of one finite volume cell, with black and white as pure streams, and gray as the mixed portion of the cell. The bottom plots are the PDFs corresponding to each of these states. [Color figure can be viewed in the online issue, which is available at wileyonlinelibrary.com.]

Eddy occurrences depend on the evolving momentum field and are related to the local turbulent kinetic energy. A given eddy of size l and location y_0, has an eddy timescale τ_e that is defined with the scaling relation $E_{\text{kin}} \approx \frac{1}{2}\rho l u \approx \frac{1}{2}\rho l^3/\tau_e^2$ for an assumed unit area domain perpendicular to the line direction y. Here, E_{kin} is a measure of the local kinetic energy,[60] and is augmented by a term $E_{\text{vp}} = \frac{1}{2}\rho v^2/l$, which is a viscous penalty term meant to suppress small eddies. Solving for τ_e yields

$$\frac{1}{\tau_e} = C\sqrt{\frac{2}{\rho l^3}(E_{\text{kin}} - ZE_{\text{vp}})} \tag{23}$$

Here, C and Z are model parameters termed the eddy rate parameter and the viscous penalty parameter, respectively. To limit the occurrence of unphysically large eddies, a large-eddy suppression mechanism is implemented such that $t > \beta\tau_e$, where β is an adjustable parameter.

Eddies are stochastically sampled and accepted on the domain during the flow evolution as follows. An eddy rate per square length is defined as $\lambda(l, y_0) = 1/(\tau_e l^2)$. Then the total rate of all eddies is $\Lambda = \int\int \lambda \mathrm{d}l\mathrm{d}y_0$ and we define the joint probability density function $P(l, y_0) = \lambda(l, y_0)/\Lambda$. In principle, eddies may be sampled from $P(l, y_0)$, and implemented as a Poisson process in time with rate Λ. However, $P(l,y_0)$ is prohibitively expensive to compute, and instead, the rejection method[61] combined with a thinning process[62] is used. Eddy occurrence times are sampled from a Poisson process with rate $1/\Delta t_s$, with the eddy size and location sampled from an analytic approximation $\tilde{P}(l, y_0)$ of $P(l,y_0)$. Candidate eddies are then accepted with probability

$$P_a = \frac{\Delta t_s}{\tau_e l^2 \tilde{P}(l, y_0)} \tag{24}$$

where Δt_s is specified adaptively to maintain an average acceptance probability of less than 0.02. Candidate eddies are sampled on the domain and the diffusion process is implemented between accepted eddies.

In the diffusive advancement portion of the solution, transport equations are solved for three velocity components, mass fractions of all elemental species in the aqueous phase, and N_{env} weights and N_{env} abscissas for each of the four calcium carbonate polymorphs. Here, $N_{\text{env}} = 4$ quadrature nodes are used for each PBE. The ODT code uses an automatically adaptive mesh in a Lagrangian finite volume formulation. The grid resolution varied between 20,000 and 50,000 for the simulations here. The transport equation for a generic scalar φ written for a grid cell is given by

$$\frac{\mathrm{d}\varphi}{\mathrm{d}t} = -\frac{1}{\rho\Delta y}(j_{\varphi,e} - j_{\varphi,e}) + \frac{S_{\rho\varphi}}{\rho} \tag{25}$$

where j_φ is the diffusive flux, $S_{\rho\varphi}$ is a source term, and subscripts e and w refer to the east and west cell faces. Here, φ is taken as u_i, Y_i, $w_{i,\alpha}/\rho$, and $R_{i,\alpha}/\rho$, that is, momentum, species mass, environment weight, and environment abscissa, each per unit mass, respectively, where α refers to a specific polymorph. In the present application, the density is assumed constant, and there is no change in the grid during the diffusive advancement.

The diffusive flux of crystal particles is assumed zero. The momentum flux terms are modeled as $j_{u_i} = -\mu \mathrm{d}u_i/\mathrm{d}y$. Central difference approximations are used to compute gradients at cell faces. Fluxes of aqueous elements are computed as $j_{Y_i} = \sum_k Y_{i,k} j_k$, where $Y_{i,k}$ is the mass fraction of element i in species k, and j_k is the mass flux of species k. Aqueous species diffusion fluxes are computed using the following relation based on the Nernst-Planck equation[63]:

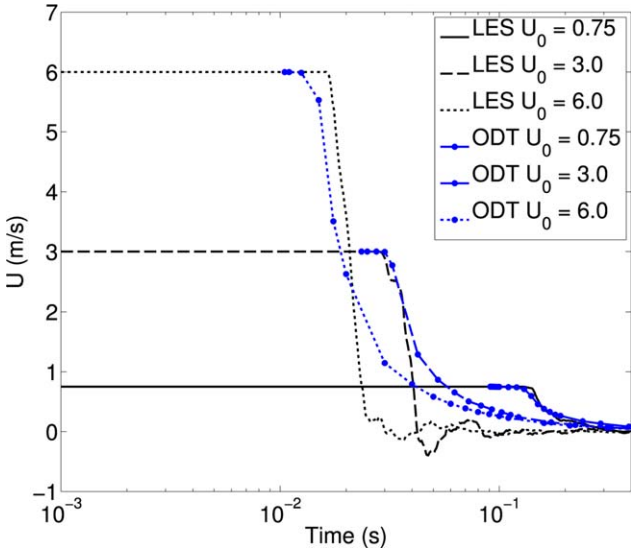

Figure 3. Spatial- (LES) and ensemble- (ODT) averaged velocity decay on centerline, with time on a semi-log scale.

Lines correspond to LES results and lines with symbols correspond to ODT results. [Color figure can be viewed in the online issue, which is available at wileyonlinelibrary.com.]

$$j_{Y_i} = -M_i \text{Đ}_i \nabla c_i + \frac{c_i z_i M_i \text{Đ}_i \sum_{j=1}^{n_{sp}-1} z_j \text{Đ}_j \nabla c_j}{\sum_{j=1}^{n_{sp}-1} c_j z_j^2 \text{Đ}_j} \tag{26}$$

where M_i is the species molecular weight, c_i is the molar concentration, z_i is the species charge number, and Đ_i is the species diffusivity. Water is taken as species n_{sp}. The species diffusivities were computed using the OLI Systems software,[64] with temperature dependence computed using the Stokes-Einstein relation.[63]

The source terms $S_{\rho\varphi}$ in Eq. 25 are zero for the momentum components. For elemental mass fractions, the source terms account for mass transfer between the aqueous phase and the solid carbonate polymorphs. For element i consisting of carbon, oxygen, and calcium

$$S_{\rho Yi} = -Y_{i,\text{CaCO}_3} \frac{4}{3}\pi \sum_{\alpha} \rho_\alpha \frac{\text{d}m_{3,\alpha}}{\text{d}t} \tag{27}$$

where Y_{i,CaCO_3} is the mass fraction of element i in calcium carbonate, and ρ_α is the density of the polymorph α. The moment equation, $\text{d}m_{k,\alpha}/\text{d}t$ (with $k = 3$ here) is the same as given above in Eq. 2 but without the mixing or convective terms.

The ODT uses a variation of QMOM that is termed direct quadrature method of moments (DQMOM),[15] in which rates for the environment weights and abscissas are written in terms of the moment sources $\text{d}m_{k,\alpha}/\text{d}t$ (again Eq. 2 without the mixing term). For a given polymorph α, the source terms $S_{w_{i,\alpha}}$ and $S_{R_{i,\alpha}}$ are computed by inverting the linear system

$$\sum_{i=1}^{N_{\text{env}}} \left[w_{i,\alpha} k R_{i,\alpha}^{k-1} S_{R_{i,\alpha}} + R_{i,\alpha}^{k} S_{w_{i,\alpha}} \right] = \frac{\text{d}m_{k,\alpha}}{\text{d}t}, \quad \text{for } k = 0 \ldots 2N_{\text{env}} - 1 \tag{28}$$

The ODT model is solved using an explicit Euler time integration. Mesh adaption is performed as given in Lignell et al.[57] When merging grid cells, the moments corresponding to environment weights and abscissas are computed and adaption is performed conservatively on these moments. The environment weights and abscissas are then reconstructed from the moments using the product-difference algorithm.[22]

Results and Discussion

Centerline data

At a similar resolution, ODT simulations take significantly less computational cost to run than the LES simulations. Due to this, the ODT simulations could be run with an increased spatial and temporal resolutions. The ODT grid resolution was increased to make the two sets of simulations have close to the same total computational cost. Specifically, the ODT was run at an order of magnitude higher than the LES in spatial resolution, and two orders of magnitude improvement in the temporal resolution. The idealized geometry used in this study is well suited to ODT's strengths. In this sense, the ODT results can considered as a baseline for analyzing the LES results.

The first thing to examine is how quickly the two streams of calcium chloride and sodium carbonate are mixed together. The centerline of the temporal jet shows a decay in the velocity over time as kinetic energy is dissipated, these results are shown in Figure 3 for both the LES and ODT results for the range of Reynolds numbers used. The LES results are spatially averaged on the centerline, while the ODT results are taken as an ensemble average over 100 ODT realizations. It should be noted that all of the results in this section are plotted with respect to a semi-log axis in time, so the mixing timescales between Reynolds numbers vary by an order of magnitude.

The LES simulations were initialized with no fluctuations, so the shear layer takes a long time period to develop the instabilities which create the eddies to mix the fluid. On the other hand, ODT undergoes stochastic processes from the start of the simulation causing the initial decay to occur much more quickly. Essentially, the ODT formulation allows for the shear layer to develop instabilities instantaneously. Due to this, the ODT results in Figure 3 were time shifted to match the LES produced velocity decay profiles as close as possible so that a direct comparison of the data can be made. This shift required larger time intervals at the lower Reynolds numbers. All subsequent data are shifted by the same timescale as this plot, the exact values of the time shifts are shown in Table 2. The velocities in Figure 3 show that the ODT velocity results decay more slowly than the results from the LES, which drop to nearly zero once the decay begins.

The centerline fluctuations of the velocity are shown in Figure 4. The LES results for the velocity fluctuations show a higher magnitude than the ODT results, however they exhibit similar trends. First, a large spike in the velocity fluctuations occurs as the first eddys are transported to the centerline. This is followed by a slow decay of these fluctuations as the kinetic energy of the system is dissipated. The larger fluctuations that occur in the LES results lead to a quick decay rate of the kinetic energy. This is the cause for the steep drop off in velocity when compared to the ODT results in Figure 3. The ODT parameters C and Z in Eq. 23 were tuned to match

Table 2. Time Shift for ODT to Match LES Timescales

Initial Velocity (m/s)	Time Shift (s)
0.75	0.091
3.0	0.0235
6.0	0.0105

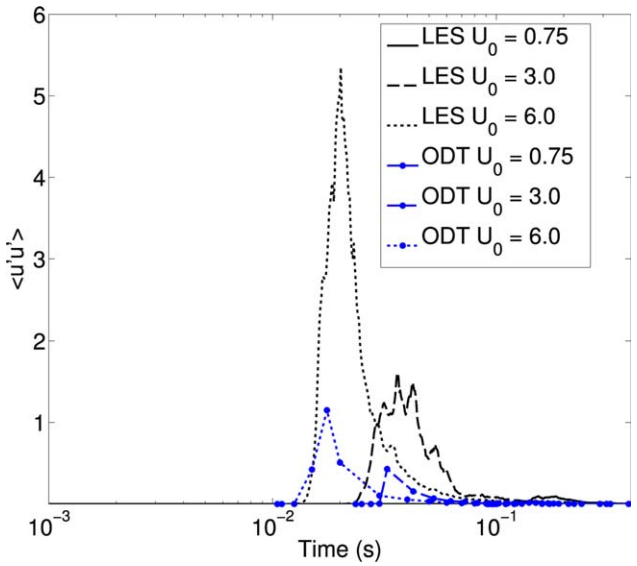

Figure 4. Spatial- (LES) and ensemble- (ODT) averaged velocity fluctuations on centerline, with time on a semi-log scale.

Lines correspond to LES results and lines with symbols correspond to ODT results. [Color figure can be viewed in the online issue, which is available at wileyonlinelibrary.com.]

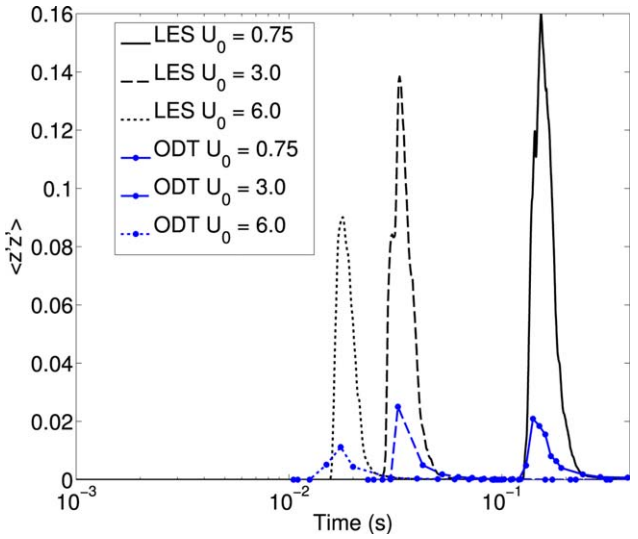

Figure 6. Spatial- (LES) and ensemble- (ODT) averaged mixture fraction variance on centerline, with time on a semi-log scale.

Lines correspond to LES results and lines with symbols correspond to ODT results. [Color figure can be viewed in the online issue, which is available at wileyonlinelibrary.com.]

the mean velocities as a priority over matching the fluctuation profiles. The tuned parameters were set at $C = 12.0$ and $Z = 0.5$. While the same trends are seen, the large magnitude difference in fluctuations was not an expected results. It is possible that the eddy suppression parameter, Z, in ODT was tuned too small and the lack of larger eddys forming limits the fluctuations of the ODT. Another possibility is that the LES is not resolving enough of the large scale flow, and the subgrid models cause the fluctuation values to be much higher than those predicted in the ODT.

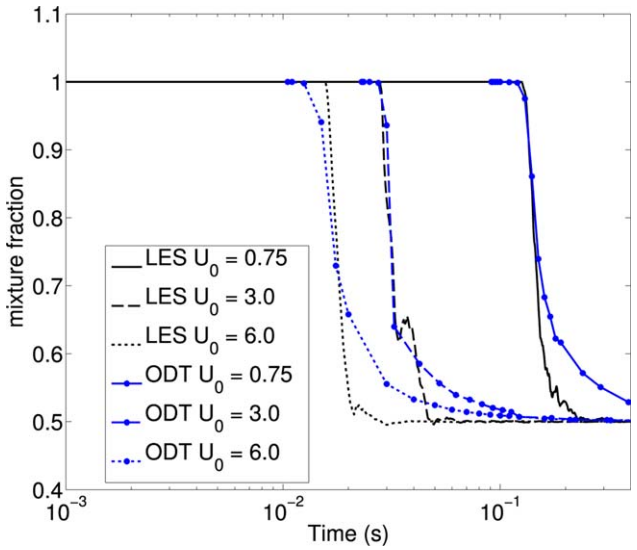

Figure 5. Spatial- (LES) and ensemble- (ODT) averaged mixture fraction on centerline, with time on a semi-log scale.

Lines correspond to LES results and lines with symbols correspond to ODT results. [Color figure can be viewed in the online issue, which is available at wileyonlinelibrary.com.]

The mixture fraction at the centerline is shown in Figure 5. All the plots start at the separated state of mixture fraction 1.0 (which is pure calcium chloride), and as the streams become mixed the mixture fraction approaches 0.5. This plot shows similar trends to those seen in the velocity decay plot. The LES results show a steep drop-off in the mixture fraction values as soon as the mixing begins to occur, while the ODT results have a slower approach to the final well-mixed state. This is especially noticeable for the lowest Reynolds number, where the LES simulation has reached the well-mixed state, but in the time period shown the ODT simulation has not yet reached this state.

The variance of the mixture fraction at the centerline is shown in Figure 6. The magnitude of the variance shows the opposite trend compared with the velocity fluctuations, increasing the Reynolds number decreases mixture fraction variance. This is intuitive, as one would expect faster scalar mixing at higher Reynolds numbers. The lowest Reynolds number case has the longest time period at which the variance remains high, this corresponds to a lower portion of the centerline at the well-mixed state during the nucleation process. This results in a lower portion of the domain reaching the highest value for the supersaturation. The spike in the fluctuations is the largest in the low Reynolds number case in the LES, so the domain in this simulation is the furthest from being entirely mixed in the early nucleation period.

As with the fluctuations in the velocity, the mixture fraction fluctuations on the centerline are higher in the LES results than in the ODT results. The faster rate of mixing in the higher Reynolds number cases results in the system reaching the highest value of supersaturation prior to the occurrence of significant nucleation. Higher supersaturation ratios result in smaller critical radii at which particles nucleate, via Eq. 5, as well as higher rates of nucleation, via Eq. 4.

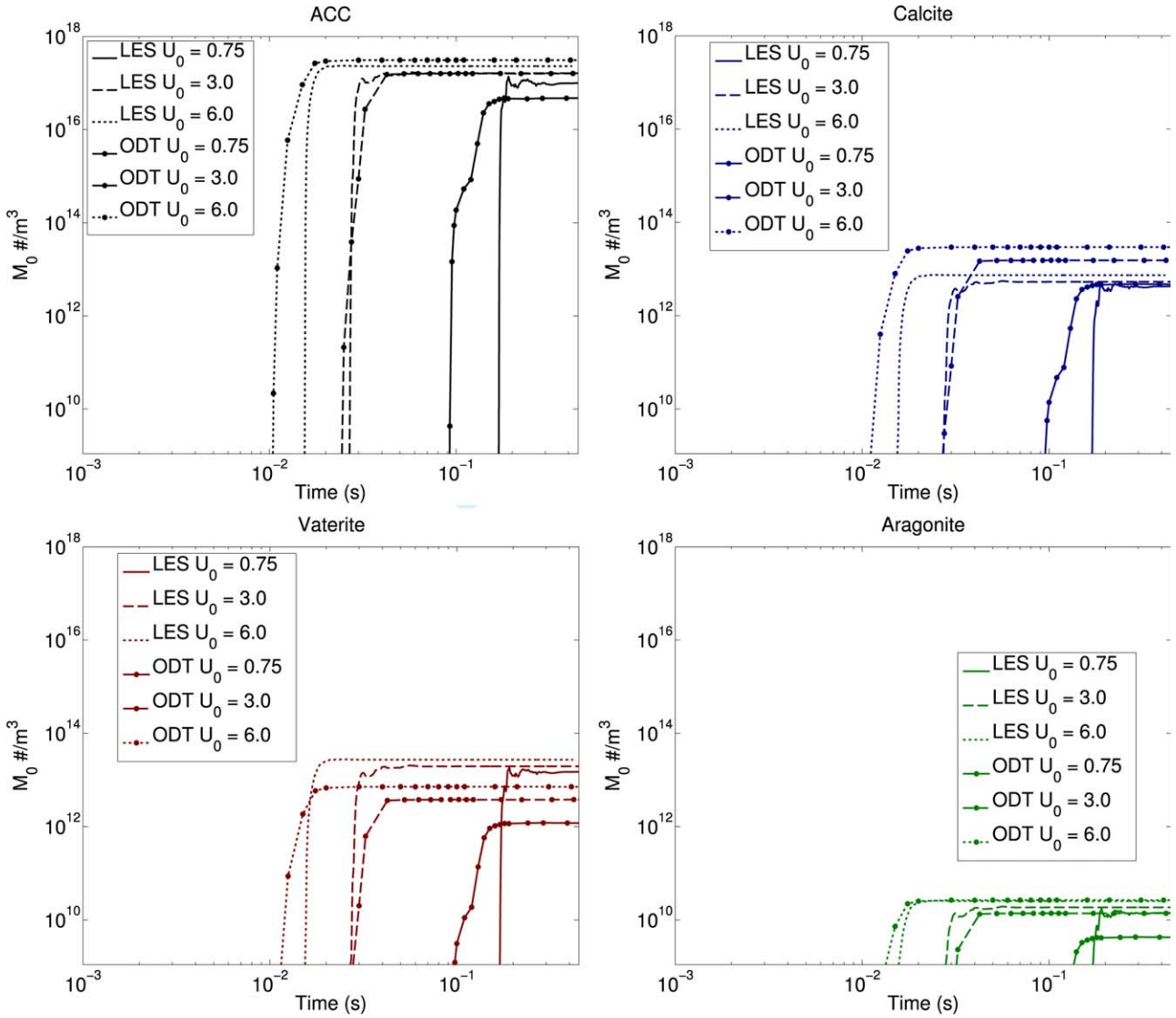

Figure 7. Spatial- (LES) and ensemble- (ODT) averaged zeroth moment (number density) on centerline, with time on a semi-log scale.

Lines correspond to LES results and lines with symbols correspond to ODT results. [Color figure can be viewed in the online issue, which is available at wileyonlinelibrary.com.]

The zeroth moment, which corresponds to the number density, for each of the four polymorphs is shown in Figure 7 for the centerline of the domain. In both sets of simulations, increasing the velocity leads to an increase in the number density of each of the polymorphs. This is the expected result, as the faster mixed systems should contain the highest supersaturation ratios, and thus the fastest nucleation rates. For ACC, the LES results at the highest Reynolds number are close, but slightly lower than the ODT results. The number density is nearly identical at the middle Reynolds number, and at the lowest Reynolds number the LES results show a higher number density than the ODT results. When looking at the plot for calcite, the LES only matches the number density of the ODT at the lowest Reynolds number, and is lower than the number density of the ODT for the two other cases. For vaterite, the LES number density is greater than that of the ODT for all three cases. The plot for aragonite shows close agreement at the highest Reynolds number, while LES values are less than the ODT in the lower velocity cases.

The first moment for each of the polymorphs is shown in Figure 8. For ACC, the same trends that were seen in the number density plot appear here with agreement between the ODT and LES methods at the middle Reynolds number. The LES results show lower values at the highest velocity and higher values at the lowest velocity. After the initial nucleation event, the data for the ACC plot levels off quickly as growth stops, the other three polymorphs all continue to grow and an increase in the first moments is seen.

Using these two lower order moments, the average radius of the the polymorphs can be calculated by dividing the first moment by the zeroth moment. The average radius of the particles on the centerline is shown in Figure 9. In order to keep the system numerically stable, a wide distribution with a low number density was seeded into the simulation. This distribution was several orders of magnitude lower than the number densities which occur from nucleation, so it has no effect on the results. However, this initial distribution results in some noise in the early time frames of the average radius plots.

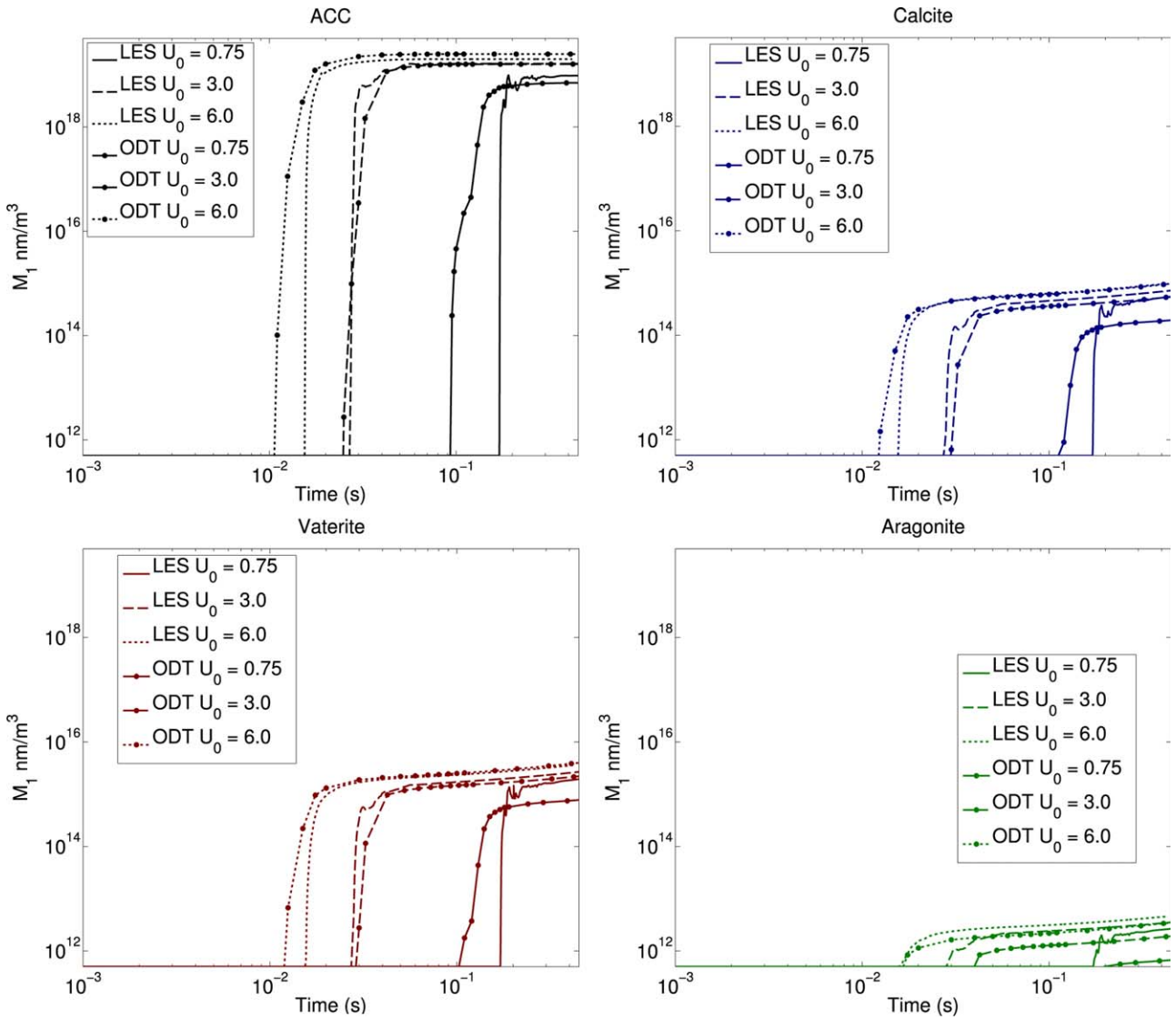

Figure 8. Spatial- (LES) and ensemble- (ODT) averaged first moment on centerline, with time on a semi-log scale.

Lines correspond to LES results and lines with symbols correspond to ODT results. [Color figure can be viewed in the online issue, which is available at wileyonlinelibrary.com.]

Once the noise is dampened, the low point in each of the curves essentially shows the radius at which particles are nucleated. After the nucleation event occurs, the increasing slope of the plots shows the growth of the particles.

For the most part, both sets of simulations show that increasing the Reynolds number of the system will lead to a decrease in the size of the nucleating particles. The ACC results show this trend well when looking at the ODT data. The differences in the particle size of the LES data are minor for ACC for the two highest Reynolds numbers. However, at the lowest Reynolds number the LES results show a lower particle size. For both sets of simulations the slope of the average radius for ACC quickly levels off. This is because the supersaturation quickly reaches near 1.0, so the growth of ACC stops. At longer timescales after mixing is complete, the ACC would begin to dissolve and transition into the other polymorphs.[16]

For the calcite plot in Figure 9, the LES simulations show significantly larger particles than those of the ODT simulations. However, the same trends show up with regards to the Reynolds number as increasing the Reynolds number decreases the particle size for the ODT results. As with ACC, the LES results only show this trend for the two highest Reynolds numbers. In both sets of simulations, the size of particles at the two highest Reynolds numbers become nearly indistinguishable. It is likely that at this high of a Reynolds number, the rate has become reaction limited, rather than mixing limited. The aragonite plot shows many of the same trends where the LES set of simulations result in larger radii than the set of ODT ones. The vaterite results show the most discrepancies, the LES results show a lower growth rate of this polymorph than what occurs in the ODT results. The results do show the same expected qualitative trend of increasing Reynolds number resulting in a decrease in particle size.

The plots shown previously pertaining to the mixture fracture can be used as an explanation for the major differences in the LES and ODT results. In Figure 5, it is seen that while the approximate time can be matched where the system goes from completely segregated to completely mixed, the time scale of this change between the two models is quite different. The LES takes a very small amount of time to reach the mixed state compared with the ODT. For the lowest Reynolds number, the ODT simulation results do not show the mixture

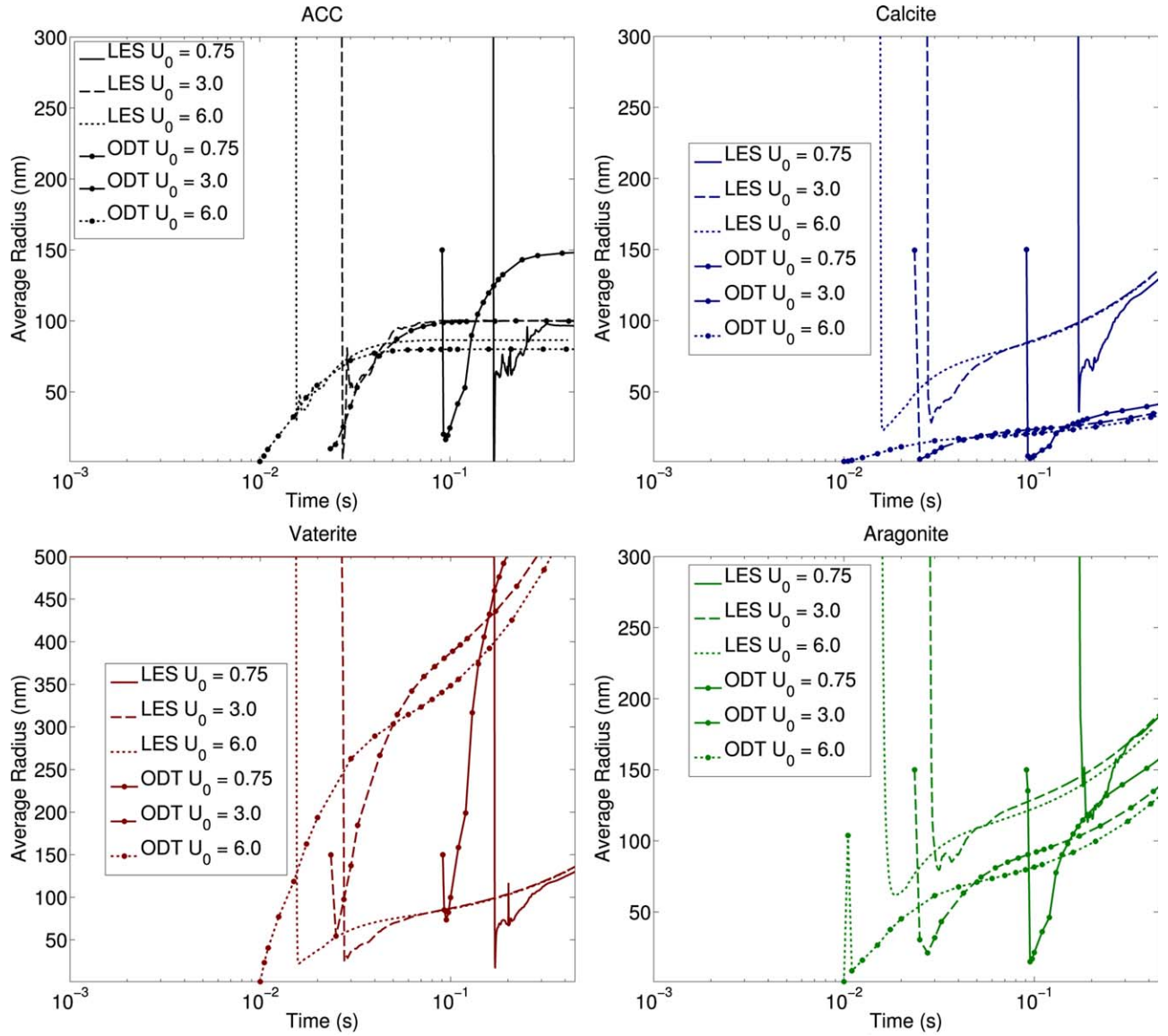

Figure 9. Spatial- (LES) and ensemble- (ODT) averaged particle radius on centerline, with time on a semi-log scale.

[Color figure can be viewed in the online issue, which is available at wileyonlinelibrary.com.]

fraction reaching the well-mixed state in the time frame shown. Since particle nucleate size decreases as supersaturation ratios increase, via Eq. 5, one would expect the LES to form smaller particles. However, except for vaterite, clearly this was not the case.

The actual cause of the discrepancies seen in the LES results are likely due to the variance of the mixture fraction. In Figure 6, all three Reynolds numbers show a significantly larger variance in the mixture fraction for the LES results in comparison to the ODT results. While the average mixture fraction may be near 0.5, the large variance means that much of the mixed portion of the domain is likely not near 0.5. For example, half could be at 0.4 while half is at 0.6, which would lead to larger particles nucleating in the LES simulations than what occur in the ODT simulations. The lowest Reynolds number case for the LES simulations showed unexpected results in the comparison, again this could be due to the large mixture fraction variance. Since Figure 6 is on a semi-log scale, the length of time the large value of the mixture fraction variance exists in the system is about 10 times longer at the low Reynolds number than at the high Reynolds number. Such large heterogeneity in the domain could be the cause of the nonintuitive results from the LES for the lowest Reynolds number.

In order to show that increasing the resolution of the LES may lead to a better comparison with the ODT results, simulations were run without the solid phase physics enabled at different grid resolutions. The centerline velocity and velocity fluctuations for the different resolutions are shown in Figure 10 for the $U_0 = 6$ m/s case. The velocity is used for this brief grid resolution study, as it was the variable used for the ODT parameter tuning. The grid resolution is varied from four times as coarse as prior results up to 25% more refined than the previous simulations. The plot for the velocity shows that the delay time in the LES before the jet mixing occurs is decreased as the resolution is increased, the smaller period in the mixing delay trends towards the result expected from the refined ODT grid. The plot for the velocity fluctuations shows the trend where an increase in the resolution leads to decreasing maximum fluctuation values. It is possible that if

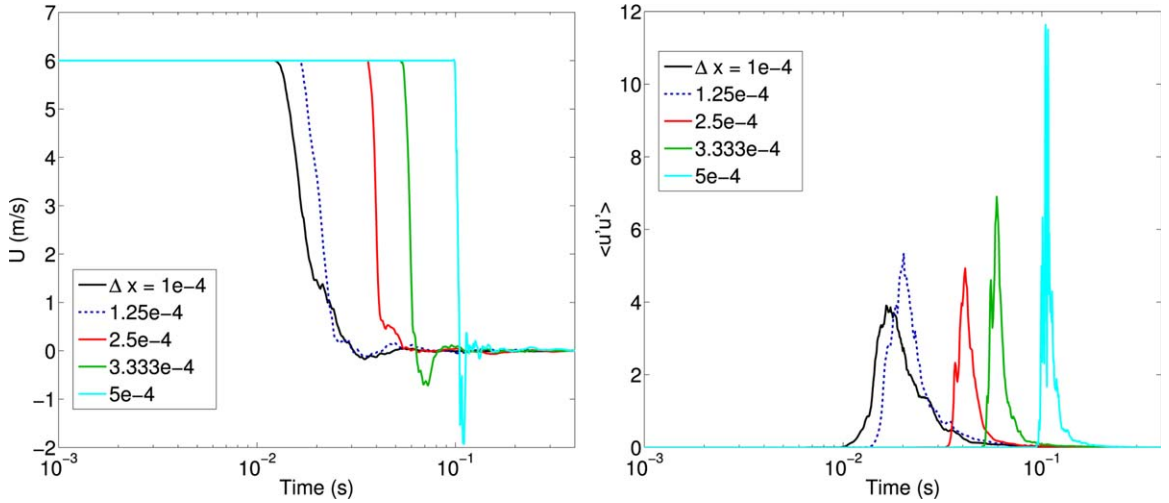

Figure 10. The velocity and velocitiy fluctuations along the centerline of the LES simulation for $U_0 = 6$ m/s as the grid resolution is increased.

[Color figure can be viewed in the online issue, which is available at wileyonlinelibrary.com.]

computing resources were available to increase the resolution further, better consistency with the ODT results may occur.

Analysis of the subgrid mixing model

The subgrid mixing model, utilized in the LES implementation, was examined by applying a filter to a set of ODT data to create a pseudo-LES type result. The filter was applied to the raw set of scalar data, and then the nucleation rates were calculated based on these filtered scalars. After creating the filtered ODT data set, the resolution of the ODT was changed and the effect of the mixing model at different grid resolutions was observed. The grid resolution was changed from 80 to 2560 grid points in the ODT domain, doubling the resolution between each simulation. The nucleation rate and ratios for ACC at differing grid resolutions are shown in Figure 11 and Figure 12, respectively. ACC was used for this analysis as this polymorph has the highest nucleation rates, and thus affects mass rate of change from aqueous to solid phase the most. The nucleation rates used in the plots are averaged over the entire ODT domain.

The nucleation rate at different time intervals of the ODT simulation is plotted in Figure 11. Each grid resolution was run both with and without the mixing model enabled. The highest grid resolution of 2560 points is assumed to be completely resolved for this analysis. Thus, as the resolution is increased, the data are assumed to converge to this value. It is shown that for early times in the system, 2.5 ms and 5 ms, the mixing model lowers the nucleation rate of the system for the lower grid resolutions, which makes it more accurate in comparison to the resolved solution. The plot here is shown with a log scale, so the difference in rates between the low and high resolution cases is significant. These early time intervals are also the most critical, as the nucleation here occurs orders of magnitude faster than the other periods of the simulation. Propagation error likely leads to less improvement seen in the later simulation times. Nucleating less mass out of the system early in the simulation, as with lower resolution cases, leads to

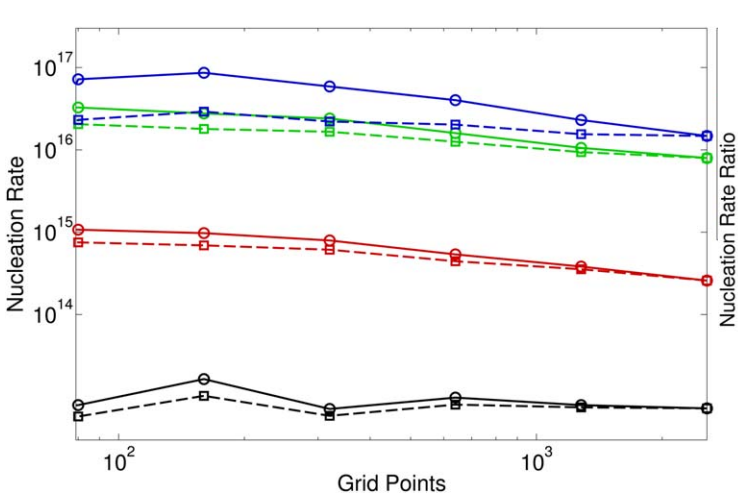

Figure 11. Nucleation rate of ACC at different grid resolutions in the ODT results.

[Color figure can be viewed in the online issue, which is available at wileyonlinelibrary.com.]

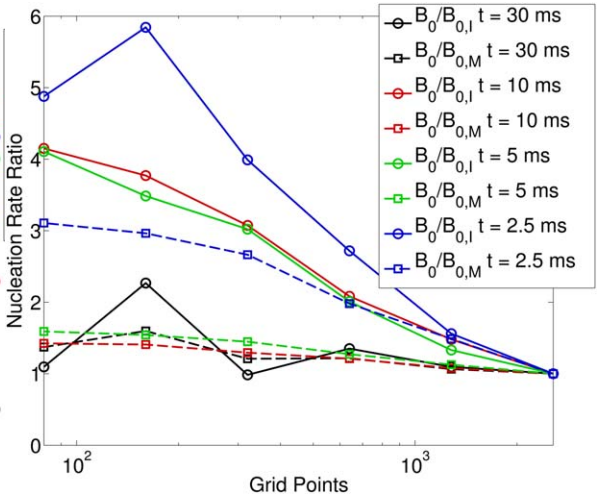

Figure 12. Nucleation rate ratios at different grid resolutions in the ODT results.

[Color figure can be viewed in the online issue, which is available at wileyonlinelibrary.com.]

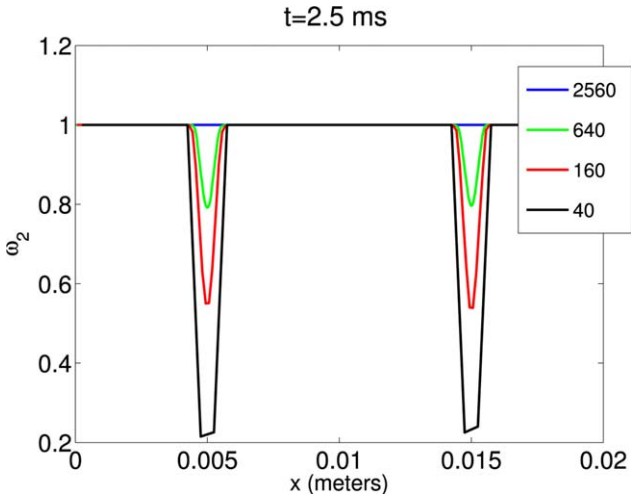

Figure 13. Central environment, ω_2, value at different grid resolutions.

[Color figure can be viewed in the online issue, which is available at wileyonlinelibrary.com.]

more mass remaining in solution at later times. This is likely the cause for $t = 10$ ms showing such little improvement compared to the improvement seen at $t = 2.5$ ms.

The ratio of the nucleation rate as a function of grid resolution to the resolved nucleation rate is shown in Figure 12. B_0 is the birth rate at a given grid resolution, $B_{0,M}$ is the birth rate at the same resolution using the mixing model, and $B_{0,I}$ is the birth rate at the resolution of 2560 grid points. The solid lines represent the factor of error when comparing the under-resolved cases to the fully resolved case. The dashed lines show the same factor with respect to the use of the mixing model in the same resolution. For example, a value of 1 would represent perfect agreement with either the full resolution, or with the mixing model. This shows that the mixing model can improve the results in the lower resolution cases, and for many of the times shown simply incorporating the mixing model provides better improvement then doubling the grid resolution.

A plot of the central environment value, ω_2, is shown in Figure 13 for the early time period of $t = 2.5$ ms, this value corresponds to the well-mixed portion of the subgrid scale. As the grid resolution is increased, the value for the second environment in the shear layer is also increased. This shows that the subgrid model behaves as it is prescribed in the theory. At low resolutions the subgrid is unmixed and the weight is low, while at high resolution the weight approaches 1, which corresponds to a perfectly mixed subgrid and fully resolved scalar field.

Conclusion

The study here presents two different sets of CFD simulations using LES and ODT methods to examine the precipitate system of calcium carbonate. The results indicate that the properties of the PSD can be manipulated by altering the Reynolds number. Specifically, increasing the mixing rate of the system results in an increase in the number density for all four polymorphs, as well as the precipitation of particles with smaller radii.

The LES code utilized a subgrid mixing model in order to account for the unresolved scales. An analysis of this subgrid mixing model was performed within the ODT framework by altering the grid size and filtering the data to create a pseudo-LES result. This analysis of the mixing model showed that it can improve accuracy in the source terms for scalar fields without increasing the grid resolution, which can be of great computational benefit. The mixing model analysis demonstrates decreasing error when utilizing the mixing model that is better in some cases than doubling the resolution, this is an excellent result for the limited computational cost of implementing this model.

Lines correspond to LES results and lines with symbols correspond to ODT results. [Color figure can be viewed in the online issue, which is available at wileyonlinelibrary.com.]

The resolution of the precipitation simulations is highlighted with a dotted line. [Color figure can be viewed in the online issue, which is available at wileyonlinelibrary.com.]

Acknowledgments

This research was sponsored by the National Nuclear Security Administration under the Accelerating Development of Retrofittable CO_2 Capture Technologies through Predictivity program through DOE Cooperative Agreement DE-NA0000740.

Literature Cited

1. Pope SB. *Turbulent Flows*. Camridge, UK: Cambridge University Press, 2000.
2. Kerstein AR. One-dimensional turbulence: model formulation and application to homogeneous turbulence, shear flows and buoyant stratified flows. *J Fluid Mech*. 1999;392:277–334.
3. Riley JJ, Metcalfe RW, Orszag SA. Direct numerical simulations of chemically reacting mixing layers. *Phys Fluids*. 1986;29:406–422.
4. Riley JJ, McMurty PA. The use of direct numerical simulation in the study of turbulent chemically reacting flows. *Turbul React Flows*. 1989:486–514.
5. Pantano C, Sarkar S, Williams F. Mixing of a conserved scalar in a turbulent reacting shear layer. *J Fluid Mech*. 2003;481:291–328.
6. Vreman B, Geurts B, Kuerten H. Large-eddy simulation of the turbulent mixing layer. *J Fluid Mech*. 1997;1997:357–390.
7. Colucci PJ, Jaberi FA, Givi P, Pope SB. Filtered density function for large eddy simulation of turbulent reacting flows. *Phys Fluids*. 1998; 2:499–515.
8. Lignell DO, Chen JH, Smith PJ. Three-dimensional direct numerical simulation of soot formation and transport in a temporally evolving nonpremixed ethylene jet flame. *Combust Flame*. 2008;155:316–333.
9. Lignell DO, Chen JH, Schmutz HA. Effects of damköhler number on flame extinction and reignition in turbulent non-premixed flames using dns. *Combust Flame*. 2011;158:949–963.
10. Punati N, Sutherland JC, Kerstein AR, Hawkes ER, Chen JH. An evaluation of the one-dimensional turbulence model: Comparison with direct numerical simulations of co/h2 jets with extinction and reignition. *Proc Combust Inst*. 2010;33:1515–1522.
11. Lignell DO, Fredline GC, Lewis AD. Comparison of one-dimensional turbulence and direct numerical simulations of soot formation and transport in a nonpremixed ethylene jet flame. *Proc Combust Inst*. 2015;35:1199–1206.
12. Ogino T, Suzuki T, Sawada K. The formation and transformation mechanism of calcium carbonate in water. *Geochim Cosmochim Acta*. 1987;51:2757–2767.
13. Plummer LN, Busenburg E. The solubilities of calcite, aragonite, and vaterite in co2-h2o solutions between 0 and 90 c, and an evaluation of the aqueous model for the system caco3-co2-h2o. *Geochim Cosmochim Acta*. 1982;46:1011–1040.
14. McGraw R. Description of aerosol dynamics by the quadrature method of moments. *Aerosol Sci Technol*. 1997;27:255–265.
15. Marchisio DL, Fox RO. Solution of population balance equations using the direct quadrature method of moments. *J Aerosol Sci*. 2005; 36:43–73.
16. Schroeder B, Harris D, Smith S, Lignell D. Theoretical framework for multiple-polymorph particle precipitation in highly supersaturated systems. *Cryst Growth Design*. 2014;14:1756–1770.

17. Davies CW. *Ion Association*. London, UK: Butterworth, 1962.
18. Randolph A, Larson MA. *Theory of Particulate Processes*. New York, US: Academic Press, 1971.
19. Chiang P, Donohue MD, Katz J. A kinetic approach to crystallization from ionic solution: Ii. crystal nucleation. *J Colloid Interface Sci*. 1988;100:203–211.
20. Steefal C, Cappellan P. A new kinetic approach to modeling water-rock interaction: the role of nucleation, precursors, and ostwald ripening. *Geochim Cosmochim Acta*. 1990;54:2657–2677.
21. Hostomsky J, Jones AG. Calcium-carbonate crystallization, agglomeration and form during continuous precipitation from solution. *J Phys D*. 1991;24:165–170.
22. Gordon RG. Error bounds in equilibrium statistical mechanics. *J Math Phys*. 1968;9:655–663.
23. Zeldovich J. Theory of the formation of a new phase cavitation. *J Exp Theor Phys*. 1942;12:525–538.
24. Kashchiev D. *Nucleation: Basic Theory with Applications*. Oxford, UK: Butterworth-Heinemann, 2000.
25. Kashchiev D, Rosmalen GM. Review: Nucleations in solutions revisited. *Cryst Res Technol*. 2003;38:555–574.
26. Dirksen J, Ring T. Fundamentals of crystallization: kinetic effects on particle size distributions and morphology. *Chem Eng Sci*. 1991;46: 2389–2427.
27. Lasaga AC. *Kinetic Theory in the Earth Sciences*. Princeton University Press, 1998.
28. Kawano J, Shimobayahi N, Kitamura M, Shinoda K, Aikawa N. Formation process of calcium carbonate from highly supersaturated solution. *J Cryst Growth*. 2002:419–423.
29. Kralj D, Brecevic L, Nielsen AE. Vaterite growth and dissolution in aqueous solution I. kinetics of crystal growth. *J Cryst Growth*. 1990; 104:793–800.
30. Kralj D, Brecevic L, Kontrec J. Vaterite growth and dissolution in aqueous solution III. kinetics of transformation. *J Cryst Growth*. 1997;177:248–257.
31. Romanek CS, Morse JW, Groassman EL. Aragonite kinetics in dilute solutions. *Aquat Geochim*. 2011;17:339–356.
32. Noguera C, Fritz B, Clemant A, Baronnet A. Nucleation, growth, and ageing scenarios in closed systems I: a unified mathematical framework for precipitation, condensation, and crystallization. *J Cryst Growth*. 2006;297:180–186.
33. Marchisio DL, Vigil RD, Fox RO. Quadrature method of moments for aggregation-breakage processes. *J Colloid Interface Sci*. 2003; 258:322–334.
34. Liew TL, Barrick JP, Hounslow M. A micro-mechanical model for the rate of aggregation during precipitation from solution. *Chem Eng Technol*. 2003;26:282–285.
35. Lin YP, Singer PC. Effects of seed material and solution composition on calcite precipitation. *Geochim Cosmochim Acta*. 2005;69: 4495–4504.
36. Stack AG, Grantham MC. Growth rate of calcite steps as a function of aqueous calcium-to-carbonate ratio: independent attachment and detachment of calcium and carbonate ions. *Cryst Growth Design*. 2010;10:1409–1413.
37. Gebrehiwet TA, Redden GD, Fujita Y, Beig MS, Smith RW. The effect of the co3 2-to ca2+ ion activity ratio on calcite precipitation kinetics and sr2+ partitioning. *Geochem Trans*. 2012;13:1.
38. Bracco JN, Stack AG, Steefel CI. Upscaling calcite growth rates from the mesoscale to the macroscale. *Environ Sci Technol*. 2013; 47:7555–7562.
39. Pokrovsky OS, Golubev SV, Schott J, Castillo A. Calcite, dolomite and magnesite dissolution kinetics in aqueous solutions at acid to circumneutral ph, 25 to 150 c and 1 to 55 atm pco2: new constraints on co2 sequestration in sedimentary basins. *Chem Geol*. 2009;265:20–32.
40. Ruiz-Agudo E, Putnis C, Rodriguez-Navarro C, Putnis A. Effect of ph on calcite growth at constant ratio and supersaturation. *Geochim Cosmochim Acta*. 2011;75:284–296.
41. Ogino T, Suzuki T, Sawada K. The rate and mechanism of polymorphic tranformation of calcium carbonate in water. *J Cryst Growth*. 1990;100:159–167.
42. Sawada K. Mechanism of crystallization and transformation of calcium carbonates. *Pure Appl Chem*. 1997;69:1997.
43. Gebauer D, Völkel A, Cölfen H. Stable prenucleation calcium carbonate clusters. *Science*. 2008;322:1819–1822.
44. Gebauer D, Cölfen H. Prenucleation clusters and non-classical nucleation. *Nano Today* 2011;6:564–584.
45. Hiemenz PC, Rajagopalan R. *Principles of Colloid and Surface Chemistry, Revised and Expanded*. New York, US: CRC Press, 1997.
46. Schlomach J, Quarch K, Kind M. Investigation of precipitation of calcium carbonate at high supersaturations. *Chem Eng Technol*. 2006;29:215–220.
47. St Germain JD, McCorquodale J, Parker S, Johnson C. Uintah: a massively parallel problem solving environment. In *High-Performance Distributed Computing*, The Ninth International Symposium, Pittsburgh, US: IEEE, 2000: 33–41.
48. Parker S. A component-based architecture for parallel multi-physics pde simulation. In *Computational Science*, Amsterdam, Netherlands: ICCS, 2002, 719–734.
49. Berzins M, Luitjens J, Meng Q, Harman T, Wight C, Peterson J. Uintah: a scalable framework for hazard analysis. In *TeraGrid Conference*, ACM, 2010, 3.
50. The University of Utah. 2014. www.uintah.utah.edu. Accessed Date: October 1, 2015.
51. Guilkey J, Harman T, Luitjens J, Schmidt J, Thornock J, de St. Germain D, Shankar S, Peterson J, Brownlee C, Reid C, Saad T, Beckvermit J, Humphrey A. *Uintah User Guide*, University of Utah: Salt Lake City, US, 2013.
52. Spinti J, Thornock J, Eddings E, Smith P, Sarofim A. Heat transfer to objects in pool fires. In *Transport Phenomena in Fires*, Southampton, UK: WIT Press, 2008.
53. Saad T, Sutherland JC, Biglari A, Abboud AW. *Wasatch Documentation*, University of Utah: Salt Lake City, US, 2013.
54. Germano M, Piomelli U, Moin P, Cabot WH. A dynamic subgrid-scale eddy viscosity model. *Phys Fluids A: Fluid Dyn*. 1991;3:1760–1765.
55. Wang L, Fox RO. Comparison of micromixing models for CFD simulation of nanoparticle formation. *AIChE J*. 2004;50:2217–2232.
56. Vedula P, Yeung PK, Fox RO. Dynamics of scalar dissipation in isotropic turbulence: a numerical and modelling study. *J Fluid Mech*. 2001;433:29–60.
57. Lignell DO, Kerstein AR, Sun G, Monson EI. Mesh adaption for efficient multiscale implementation of one-dimensional turbulence. *Theor Comput Fluid Dyn*. 2013;27:273–295.
58. Kerstein AR. Linear-eddy modelling of turbulent transport. Part 6. Microstructure of diffusive scalar mixing fields. *J Fluid Mech*. 1991; 231:361–394.
59. Kerstein AR, Ashurst WT, Wunsch S, Nilsen V. One-dimensional turbulence: vector formulation and application to free shear flows. *J Fluid Mech*. 2001;447:85–109.
60. Ashurst WT, Kerstein AR. One-dimensional turbulence: variable density formulation and application to mixing layers. *Phys Fluids*. 2005;17-025107:1–26.
61. Papoulis A, Pillai SU. *Probability, Random Variables, and Stochastic Processes*. New York: McGraw-Hillfourth, 2002.
62. Lewis PA, Shedler GS. Simulation of nonhomogeneous poisson processes by thinning. *Naval Res Logistics Quart*. 1979;26:403–413.
63. Taylor R, Krishna R. *Multicomponent Mass Transfer*. New York: Wiley, 1993.
64. OLI Systems, Inc. *OLI Systems software*, NJ, 2014.

Manuscript received Nov. 3, 2014, and revision received Apr. 9, 2015.